Finite Element Simulation Combination to Predict the Distortion of Thin Walled Milled Aluminum Workpieces as a Result of Machining Induced Residual Stresses

Daniel Weber[1]
Institute for Manufacturing Technology and Production Systems,
Technische Universität Kaiserslautern, Germany

Benjamin Kirsch
Institute for Manufacturing Technology and Production Systems,
Technische Universität Kaiserslautern, Germany

Christopher R. Chighizola
Department of Mechanical and Aerospace Engineering, University of California Davis, CA, USA

Julianne E. Jonsson
Department of Mechanical and Aerospace Engineering, University of California Davis, CA, USA

Christopher R. D'Elia
Department of Mechanical and Aerospace Engineering, University of California Davis, CA, USA

Barbara S. Linke
Department of Mechanical and Aerospace Engineering, University of California Davis, CA, USA

Michael R. Hill
Department of Mechanical and Aerospace Engineering, University of California Davis, CA, USA

Jan C. Aurich
Institute for Manufacturing Technology and Production Systems,
Technische Universität Kaiserslautern, Germany

Abstract

Machining induced residual stresses (MIRS) are a main driver for distortion of monolithic thin walled aluminum workpieces. A typical machining process for manufacturing such geometries for the aerospace industry is milling. In order to avoid high costs due to remanufacturing or part rejection, a simulation combination, consisting of two different finite element method (FEM) models, is developed to predict the part distortion due to MIRS. First, a 3D FEM cutting simulation is developed to predict the residual stresses due to machining. This simulation avoids cost intensive residual stress measurements. The milling process of the aluminum alloy AA7050-T7451 with a regular end mill is simulated. The simulation output, MIRS, forces and temperatures, is validated by face milling experiments on aluminum. The model takes mechanical dynamic effects, thermomechanical coupling, material properties and a damage law into account. Second, a subsequent finite element simulation, characterized by a static, linear elastic model, where the simulated MIRS from the cutting model are used as an input and the distortion of the workpiece is calculated, is presented. The predicted distortion is compared to an additional experiment, where a 1 mm thick wafer was removed at the milled surface of the aluminum workpiece. Furthermore, a thin walled component that represents a down scaled version of an aerospace component is manufactured and its distortion is analyzed.

The results show that MIRS could be forecasted with moderate accuracy, which leads to the conclusion that the FEM cutting model needs to be improved in order to use the MIRS for a correct prediction of the distortion with the help of the linear elastic FEM model. The linear elastic model on the other hand is able to predict the part distortion with higher accuracy when using measured data instead of MIRS from the cutting simulation.

[1] corresponding author

2nd International Conference of the DFG International Research Training Group 2057 – Physical Modeling for Virtual Manufacturing (iPMVM 2020).
Editors: Christoph Garth, Jan C. Aurich, Barbara Linke, Ralf Müller, Bahram Ravani, Gunther Weber, and Benjamin Kirsch; Article No. 11; pp. 11:1–11:21

OpenAccess Series in Informatics
OASICS Schloss Dagstuhl – Leibniz-Zentrum für Informatik, Dagstuhl Publishing, Germany

2012 ACM Subject Classification Applied computing → Physical sciences and engineering

Keywords and phrases Machining induced residual stresses, distortion, Finite element method simulation

Digital Object Identifier 10.4230/OASIcs.iPMVM.2020.11

Funding The authors would like to thank the German Research Foundation (DFG) and the National Science Foundation (NSF) for the financial support within the project AU 185/64-1 "NSF DFG Collaboration to Understand the Prime Factors Driving Distortion in Milled Aluminum Workpieces". UC Davis received funding from the NSF under Award No. 1663341 (CMMI). Any opinions, findings, and conclusions or recommendations expressed in this material are those of the authors and do not necessarily reflect the views of the NSF.

[1]Naming of specific manufacturers is done solely for the sake of completeness and does not necessarily imply an endorsement of the named companies nor that the products are necessarily the best for the purpose.

1 Introduction

The use of thin walled structural monolithic aluminum components like rib type shaped geometries is established in the aerospace industry due to their unique properties. These parts are characterized by advantages like low assembly times, high production efficiency, low production costs and good material properties like high overall-strength-to-weight ratio, high specific strength and corrosion resistance [22]. A typical machining process for such rib type shaped geometries is milling. Hereby up to 90 % of the material is removed [3]. As these components typically are long, up to 14 m, and thin walled, down to 2 mm, distortion is a common problem [3]. High costs due to remanufacturing or rejection of the parts are a result [30]. It is known that the main cause of those distortions are residual stresses (RS) [22]. They are defined as the internal stresses locked in a body, where force and torque equilibrium prevail and no thermal gradients appear [30]. In this context two types of RS are from greater interest. First, there are the RS which exist in the blank material because of former processes like heat treatments (e.g. quenching) prior to machining. These stresses are called initial bulk residual stresses (IBRS), because they appear throughout the entire part-thickness [22]. Typically, aircraft parts are machined from stress relieved aluminum alloys, e.g. AA7050-T7451, to reduce the IBRS and increase the mechanical strength [12]. The second type of RS which contribute to the distortion are the machining induced residual stresses (MIRS). They are introduced into the material during the machining process and their penetration depth is limited to a shallow surface layer of the part.

Finite element method (FEM) simulations are often used to predict the part distortion due to MIRS of milled thin walled monolithic aluminum workpieces. Mostly two different groups of FEM approaches are recognizable in the literature. Group I models are characterized by calculating the distortion of the workpiece due to the temperatures and forces of the milling process [1, 27, 33]. Furthermore, group I models considered the IBRS, milling path and clamping forces. The cutting process was hereby simplified in a way that the material removal was modeled by the element deletion of the elements along the milling path. No tool workpiece interaction was simulated. Forces and temperatures were applied to the mesh nodes while the part geometry was constrained. The temperature and force data used as input were obtained by different methods. Rai et al. e.g. calculated the forces analytically using Oxley's predictive machining theory [27]. Temperatures were determined by using the heat dissipation rate. Bi et al. used a FEM process model in DEFORM-3D[1] to simulate the

forces [1]. Furthermore, the heat was derived from the shear energy. It was assumed that the shear energy, which was calculated analytically with the help of the forces from the process model, was transformed completely into heat. Tang et al. used a FEM cutting simulation in DEFORM-3D[1] to obtain both, temperatures and forces [33]. All group I models contain a second simulation step, where the constraints were changed to allow the workpiece to deform, producing a prediction of distortion but not MIRS.

Group II models are characterized by static, linear elastic FEM simulations, where the RS are known and used as an input to predict the part distortion [3, 13, 15, 24, 25, 28]. This modelling approach only takes the final residual stress state of the machined part into account, able to consider both, MIRS and IBRS. Mostly, the stresses are applied to the finished part shape, whereas some models also consider the material removal by element deletion. The re-equilibrium of the stresses causes the workpiece to distort. The MIRS required for the simulation were mostly obtained by measured data [3, 13, 15, 25, 28] or analytical models [11, 17, 34]. Another method of gaining information on MIRS, and saving costly RS measurements, are 2D, respectively orthogonal cutting [15, 23, 26, 29], and 3D cutting simulations [16, 21, 24, 36]. 3D cutting simulations are more useful because they are able to predict the entire stress tensor including shear stresses, which are essential stresses when it comes to predicting distortion of thin walled parts [2, 7]. There are not many 3D cutting simulations that predict MIRS on aluminum workpieces available in the literature. Li et al. predicted the MIRS for milling aluminum alloy Al2024-T3 by using a cutting simulation in Third Wave Systems AdvantEdge[1] [21]. The material behavior was defined by a power law with strain hardening and thermal softening. Furthermore, a self-adaptive meshing technique was applied. As a simulation result, only the maximum compressive RS were presented and compared to measurements. However, in order to predict the part distortion accurately the full depth profile is required. Ma et al. e.g. achieved a prediction of the MIRS depth profile from milling a steel alloy by using cutting simulations in Third Wave Systems AdvantEdge[1] [24]. The Johnson-Cook material model was used. A large simulation error was stated for the comparison of distortion measurement and simulation result. Furthermore no shear stresses were presented, although they are an important factor of distortion due to MIRS [2, 7]. No validation of the MIRS in form of residual stress measurements was done.

In the present research FEM simulations of group II were investigated to predict the distortion of milled thin walled aluminum workpieces due to MIRS. The MIRS were obtained by a FEM cutting simulation for the aluminum alloy AA7050-T7451. Experiments were carried out as validation. Forces, temperatures and RS were compared to experimental data. Furthermore, the distortion of a thin wafer and a thin walled workpiece geometry was measured and compared to the model outcome. Additionally, a simulation environment in Matlab[1] was developed, which embeds both, cutting and distortion FEM simulations.

2 Methods

2.1 Experimental set up

2.1.1 Force and machining induced residual stress measurements

Down milling was carried out on a 5-axis DMG Mori DMU 70 CNC[1] machine with cemented carbide end mills. An end mill is a typical tool for machining of aerospace aluminum alloys. The tool properties can be found in Table 1.

In order to minimize the IBRS, the AA7050-T74 samples come in a stress relieved condition (T7451). The samples were cut from a large slab of stress relieved aluminum measuring 1250x1250x102 mm^3. Six blocks of material measuring 660x206x102 mm^3 were

Table 1 Tool properties.

tool properties	Kennametal[1] F3AA1200AWL
type	regular end mill (EM)
diameter	12 mm
tool holder	HSK-A 63
material	cemented carbide 10 % Co, 0.6 % Cr, 89.4 % WC max. grain size 3 µm
number of flutes z	3
helix angle	45°
cutting edge radius	-
length	76 mm
coating	-

Table 2 Machining parameters.

machining parameter	
cutting speed v_c	200 m/min
feed per tooth f_z	0.2 mm
depth of cut a_p	3 mm
width of cut a_e	4 mm
coolant	dry
direction	down milling
simulation input	SI-Unit
spindle speed $n = \frac{v_c}{\pi d}$	88 rounds/s
feed rate $v_f = f_z\ z\ n$	0.0531 m/s

saw cut from the large slab. These blocks were cut again into 15 individual plates measuring 206x102x28.5 mm^3, where the 206x102 mm^2 face was milled. The tool movement was along the negative x-direction (206 mm dimension) with respect to the sample coordinate system (see Fig. 1a).

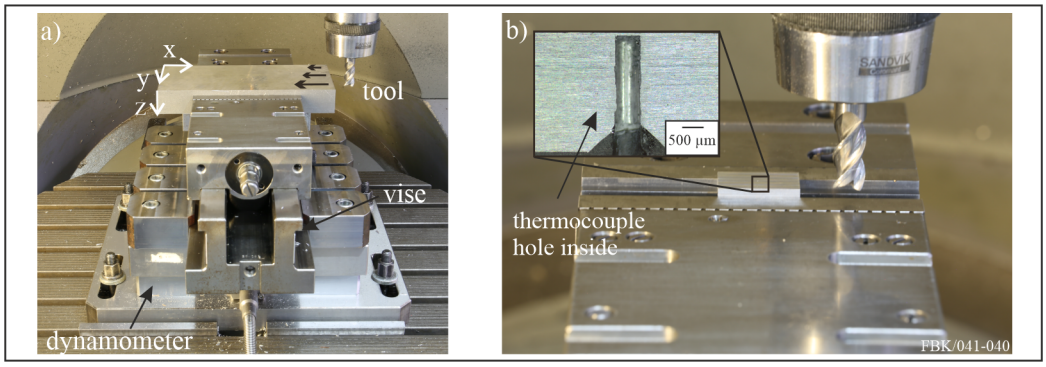

Figure 1 Experimental set up for MIRS, force (a) and temperature measurements (b).

The orthogonal feed in y-direction is along the 102 mm dimension. The machining parameters can be found in Table 2. The aluminum workpiece was clamped in a conventional vise with 125 mm long jaws and a clamping force of approximately 15 kN was applied. 5.5 mm of the workpiece height protruded prior to cutting. The process was monitored by recording forces using a piezoelectric dynamometer (Kistler Type 9255[1]) with a sampling rate of 15 kHz. One surface layer was removed, which resulted in 25 tool passes with a constant width of cut of 4 mm. The last 2 mm were removed in an additional pass, which was not included in the measurements. The three orthogonal forces (F_x, F_y, F_z), where F_x is the force in negative feed direction, F_y in orthogonal feed direction and F_z is the passive force (see Figure 1a), were analyzed. Three samples (ID 1, ID 2, ID 3) were machined to investigate the reproducibility of the MIRS.

The MIRS were measured with the hole-drilling (HD) technique following the ASTM E837-13a standard [14] on the milled 206x102x28.5 mm^3 samples. The HD technique uses a rosette strain gage to measure three components of strain while material is removed in fine increments [6]. Three components of residual stress (σ_{xx}, σ_{yy}, τ_{xy}) as a function

of cut depth are resolved from strain as a function of cut depth [14]. HD was chosen, because previous research by the authors showed that data from HD are most consistent with machining induced distortion for AA7050-T7451 parts [2]. Furthermore, multiple measurements are necessary to investigate the reproducibility of the MIRS resulting from one machining condition. Therefore, three HD measurements were conducted on the milled surface (206x102 mm^2) of each aluminum workpiece. This resulted in nine MIRS depth profiles in total. The position and depth schedule can be found in Fig. 2. The final depth of the hole was measured afterwards to compute the offset (= measured final depth – intended final depth), which was then used for a depth correction of the data (offset is then added to all depths) [2]. The analysis of the stresses is done by interpolating the nine independent measurements to the respective depth schedule in Fig. 2 and calculating the average stresses at each depth and their standard deviation at each depth.

a)

increment in mm	depth in mm
0	-
0.0127	0.0127
0.0127	0.0254
0.0127	0.0381
0.0127	0.0508
0.0127	0.0635
0.0127	0.0762
0.0127	0.0889
0.0127	0.1016
0.0127	0.1143
0.0127	0.1270
0.0254	0.1524

increment in mm	depth in mm
0.0254	0.1778
0.0254	0.2032
0.0254	0.2286
0.0254	0.2540
0.0254	0.2794
0.0508	0.3302
0.0508	0.3810
0.0508	0.4318
0.0508	0.4826
0.0508	0.5334
0.0508	0.5842

b)

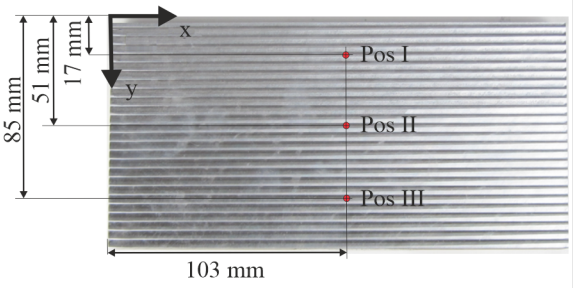

Figure 2 Depth schedule (a) and position (b) of hole-drilling measurements.

2.1.2 Temperature experiment

The temperature measurements were carried out in separate experiments on smaller AA7050-T7451 samples (30x20x9 mm^3, see Figure 1b). The sample dimensions had to be decreased in comparison to the previous experiments in order to manufacture the thermocouple hole with an accurate depth. The orientation of the tool movement was the same compared to prior experiments. The feed (negative x-) direction was along the 30 mm dimension. The sample was clamped in the vice with 4 mm of the sample height protruded prior to cutting. Thermocouples type K (1KI10TDT-40-4000MS)[1] with a diameter of 1 mm were inserted from the bottom side in the middle of the sample. The nominal distance from their end face to the cutting face was 100 µm. The temperatures at a depth of 100 µm, resulting from one cut, are not influenced by the sample size. To investigate the reproducibility, three samples (ID T1, ID T2, ID T3) were machined. The sampling rate of the temperature measurements was set to 2 kHz. The value of the maximum temperature was calculated by the arithmetic mean of 200 temperature values around the total temperature maximum of each sample (range ± 0.05 s).

2.1.3 Wafer distortion experiment

The wafer distortion experiment was designed to show the distortion potential due to the MIRS and validates the simulation model. A cube of the size 25x25x25.5 mm^3 was removed out of the larger machined sample ID 2 (206x102x25.5 mm^3) by wire electric discharge

machining (EDM). A second EDM cut was necessary to cut off a 1 mm thick wafer, including the machined surface. The distortion of the wafer was measured on the wire EDM surface (bottom) with the help of a laser profilometer. Points with a 0.2 mm spacing across the 25x25 mm^2 face of the wafer were scanned with a distance of 1 mm towards the edges.

2.1.4 Feature distortion experiment

The feature distortion experiment also served as a validation for the simulation model. Here a more complex geometry was machined. A component that resembles a down scaled version of a thin walled rib type component, which is typically used in the aerospace industry, was chosen and hereafter called feature sample. It is a small rib type component with one rib in the middle, surrounded by two pockets with a wall thickness of 3 mm (see Fig. 3).

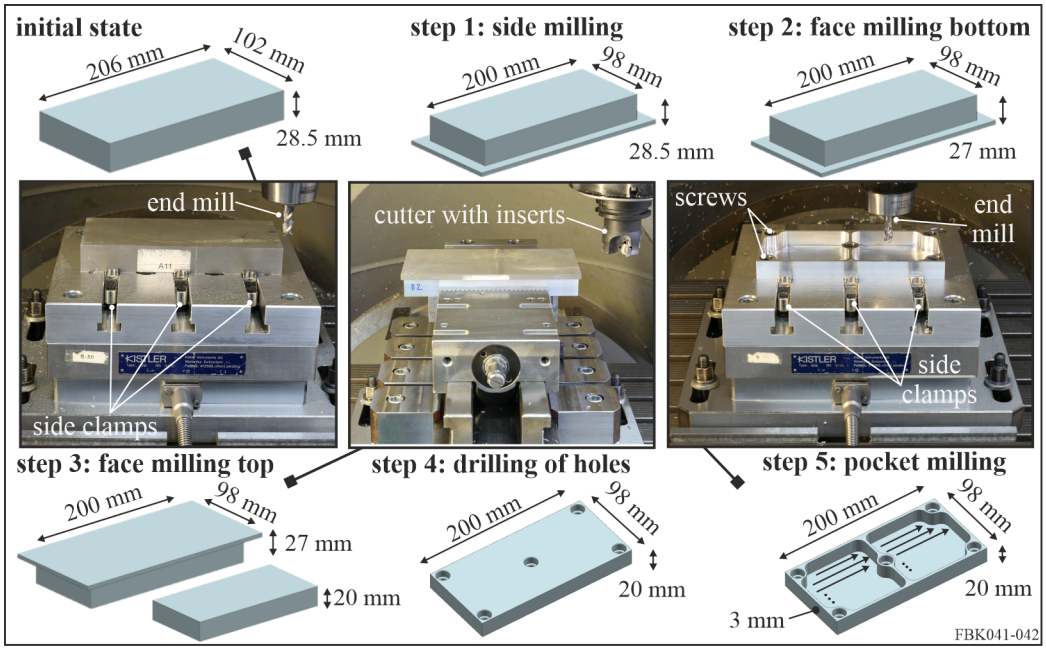

Figure 3 Machining steps of feature sample manufacturing.

The feature sample was also machined out of one of the above mentioned stress relieved AA7050-T7451 blocks with the dimensions 206x102x28.5 mm^3. Different milling operations were conducted to achieve the final geometry of the sample (200x98x20 mm^3), where about 84 % of the initial material was removed. The pockets were machined with the same machining parameters, milling strategy (zig strategy: paths from left to right, see step 5 in Fig. 3) and tool type (EM), investigated previously, where the MIRS were known. Face milling was carried out with a second tool, a cutter with indexable inserts (IDX). The tool properties can be found in Table 3. Here, the machining parameters were chosen to hardly induce any residual stresses. So, the assumption was made that only the MIRS resulting from machining the pockets contributes to the distortion of the workpiece due to MIRS.

The machining parameters can be found in Table 4. Two different clamping devices, a conventional vise and side clamps, were used (see Fig. 3). The following machining steps were executed (see Fig. 3):

1. Side milling (roughing and finishing) with EM in side clamps: 200x98x28.5 mm^3
2. Face milling bottom surface with IDX in side clamps: 200x98x27 mm^3

Table 3 Tool properties (cutter with indexable inserts).

tool properties	Sandvik[1] R590-050HA6-11M
type	cutter with indexable inserts (R590-110504H-NL H10)[1]
diameter	50 mm
tool holder	HSK-A 63
material	cemented carbide
number of inserts z	2
major cutting edge angle	90°
cutting edge radius	0.4 mm
functional length	71 mm
coating	-

3. Reclamping sample upside down in vise, face milling (IDX) top surface: 200x98x20 mm^3
4. Drilling of holes with 9 mm drill
5. Reclamping in side clamps and screws and milling of pockets (zig strategy with alternating milling of pocket layers) with EM

Table 4 Machining parameters for manufacturing the feature sample.

machining parameter	side milling (EM) step 1	face milling (IDX) step 2 and 3	pocket milling (EM) step 5
cutting speed v_c	450 m/min	730 m/min	200 m/min
feed per tooth f_z	0.055 mm	0.2 mm	0.2 mm
depth of cut a_p	5x 4.4 mm (roughing) 22 mm (finishing)	1.5 mm (bottom); 5x 1.4 mm (top)	3 mm
width of cut a_e	2.5 mm (roughing) 0.5 mm (finishing)	40 mm	4 mm

Side clamps and screws were chosen for clamping while milling the pockets to prevent the bottom surface from distortion before the workpiece was completely finished. Finally, the distortion of the bottom surface at the backside was measured with the coordinate measuring machine Tesa micro hite 3D DCC[1] with a repeatability limit (ISO MPE-p) of 3.5 µm. A spacing of the measured points of 2 mm was chosen with a distance of 1 mm to the edges.

2.2 Simulation model

The simulation combination to predict distortion of milled thin walled aluminum workpieces due to MIRS consists mainly of two different FEM models, embedded in an Matlab[1] environment (see Fig. 4). The two FEM models are a 3D, dynamic, elastic-plastic cutting simulation and a 3D, static, linear elastic FEM model [37]. The cutting model simulates the tool workpiece interaction and predicts the MIRS due to the machining parameters (input). With the help of the linear elastic model the MIRS from the previous model are applied at the workpiece to forecast the part distortion. Both FEM models are modelled and calculated in ABAQUS[1]. The link between the two models, extracting the MIRS depth profile and applying it automatically to the boundary layer of the workpiece of the second model, is handled by a developed Matlab[1] script (see Fig. 4).

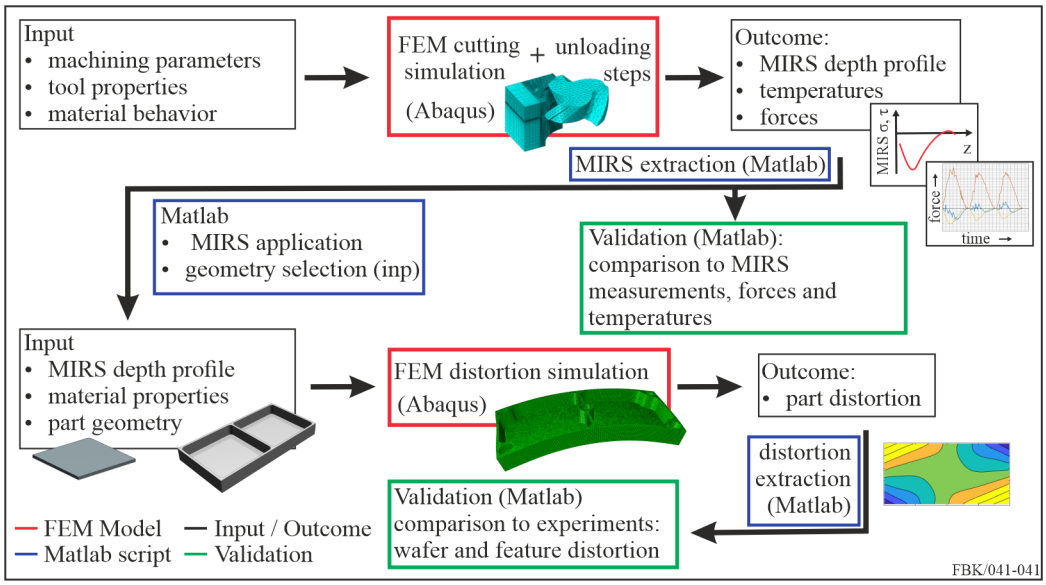

Figure 4 Simulation combination: Two FEM models embedded in Matlab[1] environment.

2.2.1 3D dynamic FEM cutting model

The required information on the MIRS resulting from milling are obtained by a 3D FEM cutting simulation, which is set up in ABAQUS[1]. An explicit, dynamic, elastic-plastic approach is chosen. An explicit solver is used, because the modelling of the complex contact problem requires the application of an explicit solver. This is very efficient for simulating highly non-linear problems involving large localized deformations, high strain rates and changing contact conditions as those experienced in the cutting process [38]. As input data the machining parameters feed rate v_f and rotation speed n are given in SI-Units (see Table 2). Only one rotation of the tool, which lasts 0.0113 s, was computed due to large computational times. The tool is assumed as a rigid body, neglecting wear. Rigid body is an acceptable assumption, because of the significantly high elastic modulus of the cemented carbide tool and the resulting low elastic deflection of it compared to the large plastic deformation of the aluminum workpiece. Neglecting wear is an acceptable assumption, because only one rotation of the tool is simulated. A thermomechanical analysis is chosen to consider both, mechanical and thermal effects. Furthermore, the tool is shortened to a length of 5 mm. The workpiece is a 10x8x15 mm^3 block with a circular cutout of the size of the tool radius (6 mm). The workpiece used in the cutting simulation is way smaller than a typical rib type component or the workpiece used for the milling experiments (see Fig. 5) to reduce the number of elements and save computational costs, because cutting simulations need a high computational time.

The mesh consists of 760,919 eight-node thermally coupled brick, trilinear displacement and temperature elements with reduced integration (C3D8RT). A fine mesh in the cutting zone, especially in the near surface region, is necessary to resolve the MIRS depth profile accurately. Here the dimensions of the elements are 50x20x20 µm^3 (see Fig. 6). The workpiece is hold in place with the help of fixture boundary conditions (BC), which set all degrees of freedom to 0 at the faces marked in Fig.6 [32]. Furthermore, the movement in x- and y- direction of the nodes on the arc surface are constrained, because in reality the circular cutout would be filled with material. The tool consists of 29,217 four-node thermally coupled tetrahedron, linear displacement and temperature elements (C3D4T) with a global element size of 0.5 mm and a finer mesh near the cutting edge (see Fig. 6).

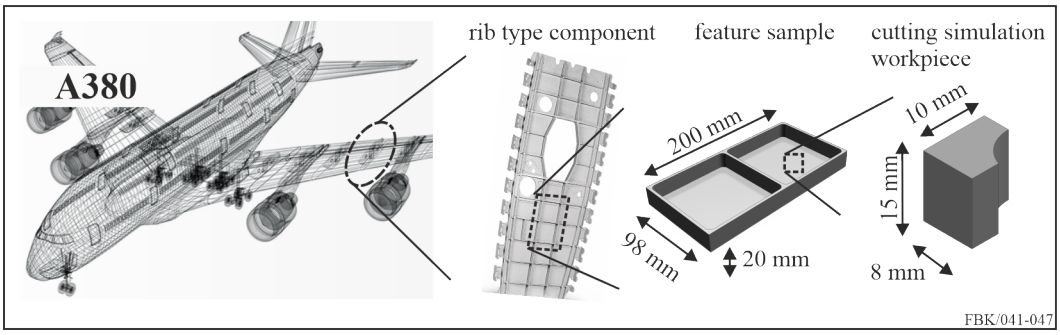

Figure 5 Different dimensions of real assembly, part and workpieces used for simulations [9, 10, 37].

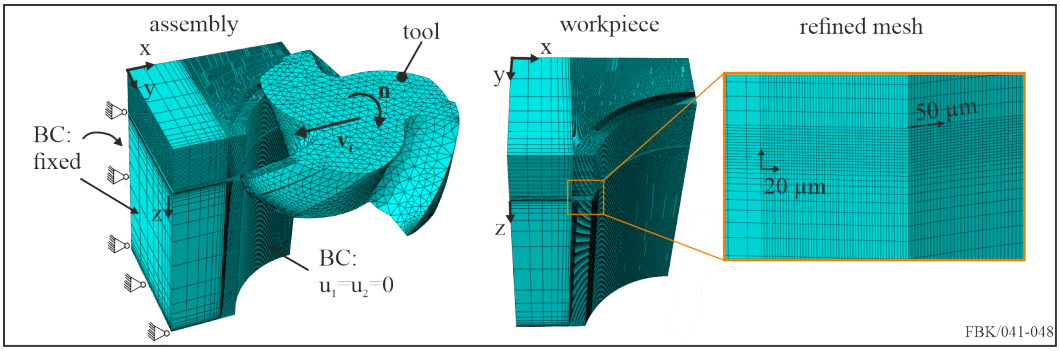

Figure 6 Mesh of tool and workpiece.

The material behavior of the workpiece is described via the Johnson-Cook strain rate dependence material model, where the yield stress at nonzero strain rate $\bar{\sigma}$ of the material is defined according to Eq.(1) [19].

$$\bar{\sigma} = \left[A + B\left(\bar{\varepsilon}^{pl}\right)^{n}\right]\left[1 + C\,\ln\left(\frac{\dot{\bar{\varepsilon}}^{pl}}{\dot{\epsilon}_0}\right)\right]\left(1 - \frac{T - T_{trans}}{T_{melt} - T_{trans}}\right) \tag{1}$$

In Eq.(1) $\bar{\varepsilon}^{pl}$ is the equivalent plastic strain, $\dot{\bar{\varepsilon}}^{pl}$ is the equivalent plastic strain rate and $\dot{\varepsilon}_0$ is the reference plastic strain rate, which is commonly assumed to be 1 [32]. The temperatures T, T_{melt} and T_{trans} are the prevailing temperature, the melting temperature and the transition temperature. A, B, C, m and n are material parameters. n and m are the strain hardening coefficient, respectively the thermal softening coefficient. A, B and C describe the yield stress behavior. The Johnson-Cook material parameters for AA7050-T7451 used in the present research are listed in Table 5 [35]. The start of material damage is modelled via the Johnson-Cook damage initiation criterion, which is a special case of the ductile criterion [32]. Damage happens when the criterion for damage initiation is met (Eq.2).

$$\omega_D = \int \frac{d\bar{\varepsilon}^{pl}}{\bar{\varepsilon}^{pl}_D(\eta, \dot{\varepsilon}^{pl})} = 1, \tag{2}$$

where ω_D is a state variable, η is the stress triaxiality $\eta = -p/q$ with pressure stress $p = -\,tr\,\boldsymbol{\sigma}$ (Cauchy stress tensor $\boldsymbol{\sigma}$) and Mises equivalent stress $q = \sqrt{\frac{3}{2}\boldsymbol{\sigma}^D \cdot \boldsymbol{\sigma}^D}$ (stress deviator $\boldsymbol{\sigma}^D$) and the equivalent plastic strain at the onset of damage $\bar{\varepsilon}^{pl}_D$, which is defined according to

Eq.(3) [19].

$$\bar{\epsilon}_D^{pl} = \left[d_1 + d_2 \exp\left(d_3 \frac{p}{q}\right)\right]\left[1 + d_4 \ln\left(\frac{\dot{\bar{\varepsilon}}^{pl}}{\dot{\varepsilon}_0}\right)\right]\left(1 + d_5 \frac{T - T_{trans}}{T_{melt} - T_{trans}}\right) \tag{3}$$

In Eq.3 d_1 to d_5 are the Johnson-Cook damage parameters (see Table 6) [20].

Table 5 Johnson-Cook material parameter for aluminum alloy AA7050-T7451 [35].

A	B	C	m	n	T_{melt}	T_{trans}	$\dot{\varepsilon}_0$
490 MPa	207 MPa	0.005	1.8	0.344	600 °C	20 °C	1

Table 6 Johnson-Cook damage parameter [20].

d_1	d_2	d_3	d_4	d_5	T_{melt}	T_{trans}	$\dot{\varepsilon}_0$
-0.77	1.45	-0.47	0	1.6	600 °C	20 °C	1

The damage evolution is characterized by a damage evolution law based on the linear displacement of the elements. The effective plastic displacement $\bar{u}_f^{pl}$ is described via the evolution Eq.(4).

$$\dot{\bar{u}}^{pl} = L\dot{\bar{\epsilon}}^{pl}, \tag{4}$$

where L is defined as the characteristic length of the element [32]. The damage variable is a function of the equivalent plastic displacement $d = d(\bar{u}^{pl})$. A linear evolution of the damage variable is chosen, Eq.(5).

$$\dot{d} = \frac{L\dot{\bar{\epsilon}}^{pl}}{\bar{u}_f^{pl}} = \frac{\dot{\bar{u}}^{pl}}{\bar{u}_f^{pl}} \tag{5}$$

Final failure is defined when the effective plastic displacement $\bar{u}^{pl}$ reaches the specified effective plastic displacement at point of failure ($\bar{u}^{pl} = \bar{u}_f^{pl}$), which is here defined by the smallest element length of 20 µm. At this point element deletion takes place and allows for the separation of the material, respectively the chip formation. Element deletion is realized by setting the stiffness matrix at the affected element to 0 ($d = 1$ fully degraded). The entire material behavior is summarized by Figure 7a. Besides the Johnson-Cook material parameters, more mechanical and thermal material parameters, e.g. density and Young's modulus, for workpiece and tool need to be defined (see Table 7). Heat is caused by the deformation of the material involving high inelastic strains [31]. This is modeled by a volumetric heat flux defined via the inelastic heat fracture β option in ABAQUS[1]. It is assumed that 90 % of the energy caused by deformation is converted into thermal energy [23]. Furthermore, it is defined, that all of the dissipated energy due to friction is released as heat and a surface film condition enables the heat convection from the model surfaces to the surrounding air [31].

The contact between workpiece and tool was modelled via general contact interaction. Therefore, a surface with all workpiece elements (exterior and interior entities) was defined. Coulomb friction was applied. In the literature there is no agreement on the friction coefficient between a cemented carbide tool and an aluminum alloy workpiece found [5]. Here a friction coefficient µ of 0.3 was chosen [18]. The simulation was run on the high-performance computer

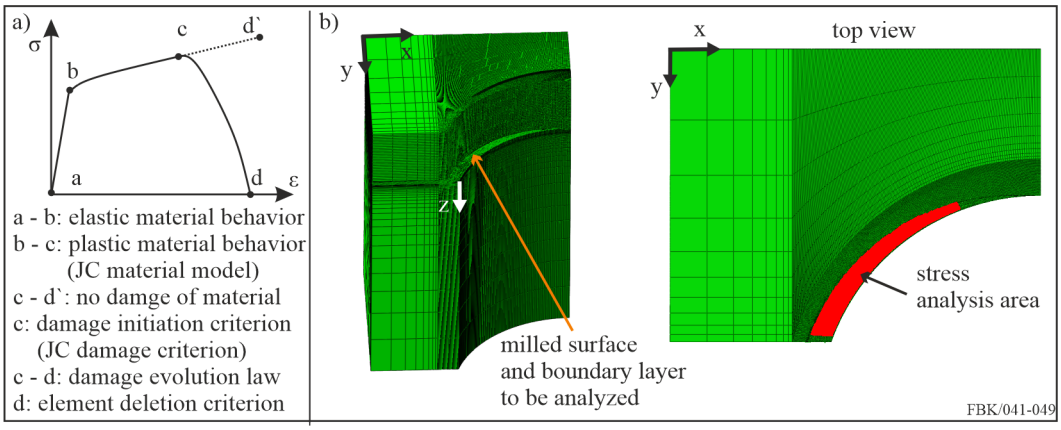

Figure 7 Typical uniaxial stress-strain response of a metal specimen (according to [32]) (a) and deformed workpiece with highlighted residual stress analysis area (b).

Table 7 Material parameters for workpiece and tool.

material properties	workpiece	tool
density ρ in kg/m^3	2,830	15,000
Young's modulus E in MPa	71,700	640,000
Poisson ratio ν	0.33	0.22
thermal expansion coefficient α in 1/K	25.5E-6	6E-6
thermal conductivity coefficient k in W/(m K)	157	55
specific heat capacity c_p in J/kg°C	860	240
inelastic heat fracture β	0.9	-
film coefficient h in W/(m^{2}K)	80	-

"Elwetritsch" at the TU Kaiserslautern with a computational time of 7 days. Besides the cutting simulation itself, unloading steps after the cutting process are necessary to guarantee that the residual stresses are in equilibrium. Two unloading steps were executed in a second simulation: The deformed mesh of the workpiece along with the information on stresses and temperatures were imported (via Matlab[1]) in a new ABAQUS[1] FEM model, which simulated the process of cooling down the workpiece to room temperature and releasing the fixture BC. At the end the MIRS were analyzed with a developed Matlab[1] script. Therefore, the stresses at all nodes of the area marked in Fig. 7b, at the milled surface and in the boundary layer of it, were extracted and averaged for each depth. Furthermore, the standard deviation was computed for each depth and discussed together with the residual stress results in section 3.3.

2.2.2 3D Static, linear elastic FEM model

A static, linear elastic finite element model was set up in ABAQUS[1] to simulate the distortion due to the MIRS. The MIRS (σ_{xx}, σ_{yy}, τ_{xy}) extracted from the cutting model and the measured MIRS (as validation) respectively, were implemented as an input and the distortion was calculated, after equilibrium had been set. Plane stress with $\sigma_{zz} = 0$, $\sigma_{xz} = 0$, and $\sigma_{yz} = 0$ was assumed. The geometries were, according to the wafer, a 25x25x1 mm^3 thin plate (see Fig. 8a), and the thin walled feature sample (see Fig. 8b).

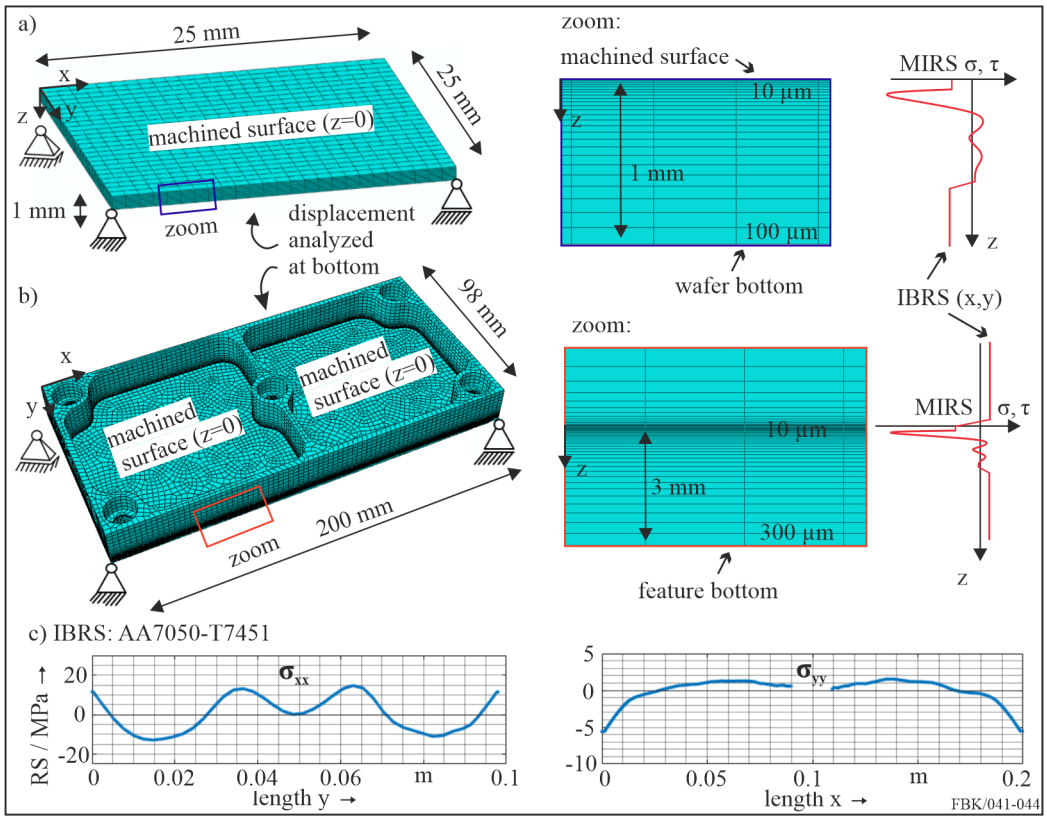

Figure 8 Wafer (a) and feature linear elastic FEM model (b), and measured IBRS (c).

The z-direction corresponds to the depth of the MIRS. The MIRS were linearly interpolated over depth z at the element centroids and applied as an initial condition on the entire milled surface of the wafer and on the bottom surface of the pockets of the feature sample. For depths smaller than the first interpolated point the first interpolated MIRS was used (see Fig. 8). For depths greater than the last measured depth the IBRS, which were left over in the blank material after the stress relief process, are used. They were measured using the slitting method prior to milling (see Fig. 8c) [8]. The IBRS depend on the x- and y- position. The stresses applied at the centroids were linearly interpolated accordingly to their coordinates. The mesh of both geometries consisted of eight-node brick elements (C3D8) with 62,500 elements in total for the wafer and 152,936 elements for the feature sample. The global size of the elements for the wafer geometry was set to 500 µm. Due to the larger geometry of the feature sample the global size of the elements was set to 2.5 mm. There were 25 elements in z-direction of the wafer with the smallest size of 10 µm at the machined surface and bigger elements at the bottom face (100 µm) (see Fig. 8), in order to precisely resolve the residual stresses near the surface and still reduce the total number of elements for calculation time reasons. Due to the larger thickness of the bottom of the feature sample (3 mm) compared to the wafer the smallest size of 10 µm increased to the bottom to 300 µm. Both parts, wafer and feature, were constraint by the 3-2-1 constrain principle, which avoided rigid body motion, but enabled a free distortion of the bodies [1]. Linear elastic material behavior with a Young's modulus of 71,700 MPa and a Poisson ratio ν of 0.33 was given. After equilibrium was calculated, the displacement at the bottom was analyzed and compared to the wafer and feature experimental distortion.

3 Results and discussion

First, the results of the FEM cutting simulation are discussed in terms of force, temperature, MIRS and compared to experimental data (see section 3.1-3.3). Second, the outcome of the subsequent FEM model, which predicts the distortion, is discussed and compared to the wafer and feature distortion experiments (see section 3.4.1, 3.4.2).

3.1 Force analysis

The forces F_x, F_y and F_z of the simulation and the experiments can be found in Fig. 9a. One rotation of the tool (t=0.013 s), which means three cutting edge engagements, is illustrated. The forces of the experiment were extracted from the force signal of pass 14 of sample ID 1.

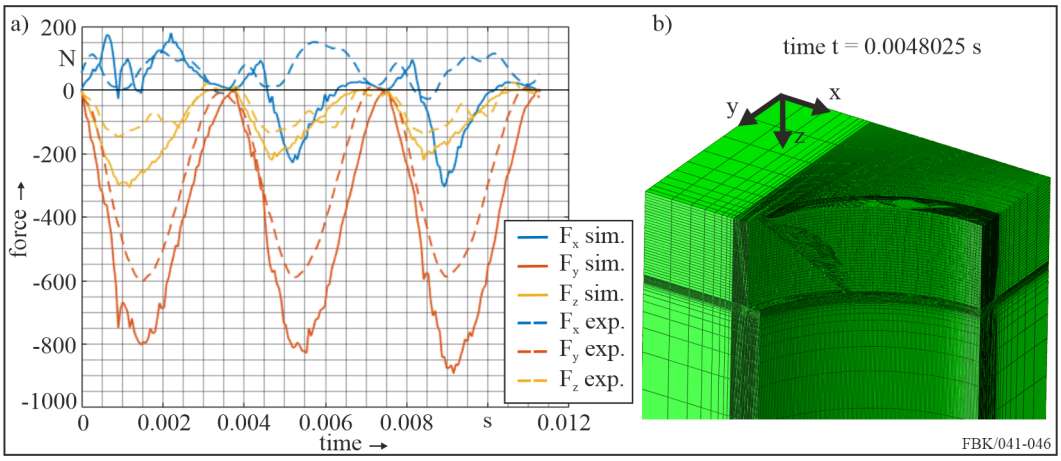

Figure 9 Force comparison of simulation and experiment (a) and simulated chip formation (b).

The three peaks for each force component correspond to the engagement of each of the three flutes. Forces F_y are the highest in magnitude, because this is the direction where the primary cutting happens (see Fig. 9b). The experimental force $F_{y_{exp}}$ shows a maximum magnitude of 600 N. The simulation force $F_{y_{sim}}$ overcomes this maximum. Its highest magnitude is about 800 N for the fist two engagements and 865 N for the last engagement. A similar trend occurs for the forces in z-direction. The maximum magnitude of $F_{z_{sim}}$ is higher than measured in experiments (200 N compared to 140 N). F_x shows positive and negative values because of the superposition of the cutting of the cutting edge and the pushing of the major flank face in the other direction. The comparison of forces F_x shows that the trend of the experimental force signal is only matched for the first engagement, where a similar magnitude is reached. The forces of the second and third cut are mostly negative, which indicates that the effect of pushing of the major flank face is dominating in the simulation. The magnitude of the different simulated forces for the different engagements differs from each other, because of multiple reasons. First there is more material removed for the first cut compared to the others due to the geometry of the chip. The first chip does not represent the actual chip form, since the initial geometry has a cutout of a perfect circle with a radius of 6 mm. Second, the simulation does not account for a continuous chip. Often elements of the chip were deleted due to the element deletion criterion, which tears the chip into several smaller parts. However, it can be stated that forces of simulation and experiment agree to a certain level. Differences in experimental and simulated forces might be because of the absence of elastic effects from the tool being in contact with the workpiece

and machining vibrations, which occur during real machining. Furthermore, the parameters used for describing the plastic material behavior and damage of the material are literature values, which may not suit best for the used aluminum alloy.

3.2 Temperature analysis

The temperature of the simulation is analyzed at the node N_T, which is located on the third cross-section of the undeformed chip, 110 µm underneath the milled surface (see Fig. 10a). After 0.008249 s the third flute's cutting edge just passed the node N_T and the maximum temperature $T_{spot_{max}}$ of 40.05 °C is reached (see Fig. 10b). The other two local maxima in the temperature profile resulted from the first two engagements of the tool.

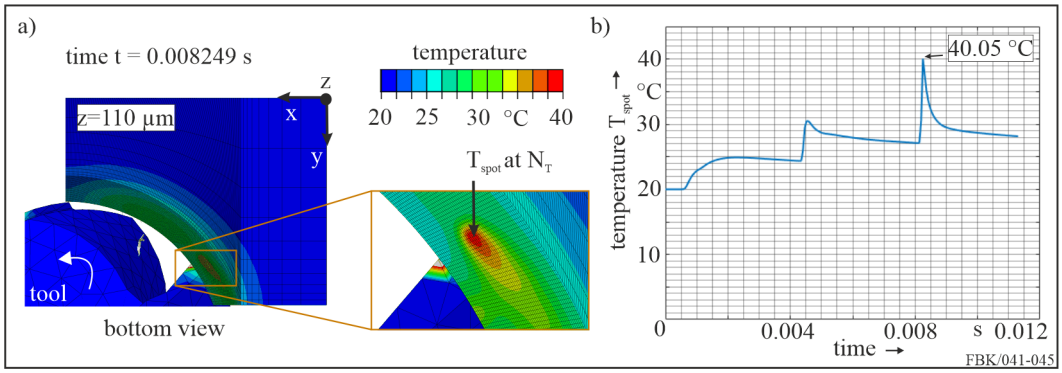

Figure 10 Position of temperature analysis (a) and the temp. profile over time at node N_T (b).

The maximum temperature of the milling experiments can be found in Table 8. The max. temperature is reached shortly after the tool moved over the thermocouple. The average value of three maximum temperatures (ID T1, ID T2, ID T3) is 32.2 °C. The temperatures of both simulation and experiment are on a similar level and agree well. One reason why the experimental temperature is slightly lower could be that the sampling rate of 2 kHz of the thermocouple is not enough to resolve the temperature profile in the same way the simulation does (15 kHz). Furthermore, the heat conduction in reality between the thermocouple face and the workpiece has to be considered, although a heat-conducting paste was used.

Table 8 Experimental measured maximum temperatures.

maximum temperature sample ID T1	maximum temperature sample ID T2	maximum temperature sample ID T3	average max. temperature
33.6 °C	31.7 °C	31.4 °C	32.2 °C

3.3 Machining induced residual stress analysis

The simulated and measured MIRS are compared in Fig. 11. All MIRS follow a square root-shaped stress profile with a pronounced maximum of residual stress (MaxRS), which is defined here as the highest absolute value of RS including compressive (negative) RS as well. This depth profile is typical for MIRS from milling [22].

The simulated normal MIRS at shallow depths (first extracted measured depth) are tensile, followed by a layer of compressive RS, whereas the shear RS are consistently negative. After the MaxRS is reached, the stress profiles of all three components increase and get to

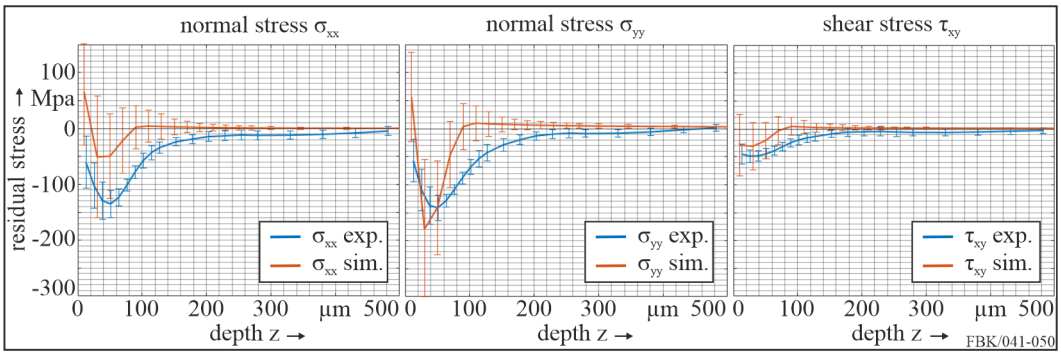

Figure 11 Comparison of MIRS from simulation and experiment.

0 MPa at about 90±20 µm (normal stresses) and 70±20 µm (shear stress). The measured MIRS show a similar behavior, except that the first measured normal RS is compressive and the MIRS are driven deeper into the material. The experimental MIRS reach 0 MPa at about 230±20 µm. The simulated MaxRS in y-direction and its depth are on a similar level compared to measurements. MaxRS_{yy} of the simulation is -180±124 MPa at 30 µm compard to -140±23 MPa at 50 µm in experiments. The simulated RS in x-direction are smaller in magnitude. The simulated MaxRS_{xx} is -50±76 MPa at a depth of 50 µm compared to -136±24 MPa at a depth of 50 µm in the experiments. The behavior of different MaxRS for y- and x-direction could be explained by the forces, which also show differences in their maximum magnitude (see section 3.4.2). In addition the simulated forces in y-direction match measured forces better than in x- direction. The simulated shear RS are lower in magnitude with MaxRS_{xy} -31±42 MPa at 30 µm compared to measurements -49±12 MPa at 25 µm. It is noticeable that the standard deviations (STD) of the simulated MIRS are high, especially for shallow depth smaller than 50 µm. The STD of the first extracted depth (10 µm) is the biggest, because the majority of the elements of the first layer were deleted. The few remaining ones were not deleted properly during the first cut, leaving distorted elements behind. This resulted not only in a high STD, but also in an area of high tensile RS near the surface (see Fig. 12). That means that the RS of the first extracted point are not representative and will be excluded for further use in section 3.4.1. The reason for the high STD of the following depth layers is the inhomogeneous distribution of RS (see Fig. 12) in the cutting area due to the influences of boundary conditions and chip formation process [36] (see Fig. 12). The differences between simulation and experiment might be explained by the absence of the run out of the tool (movement of the tool over the milled surface) in the simulation, which does not happen because only one rotation of the tool is simulated. This also leads to the undesirable effect that the stress analysis area is close to the workpiece edges. Also, the effect of multiple machining passes in orthogonal feed direction on the MIRS is not covered by the simulation. Furthermore, the material behavior and friction modelling is based on literature values, which might not be accurate for the used material. Besides the mesh, the stable time increment and boundary conditions could influence the results.

In general, it can be stated that the typical depth profile with compressive RS is represented by the simulation on average. Especially the profile of shear RS and the depth of MaxRS agree well with measured data. Differences are found for the MaxRS and for the thickness of the RS layer with measured data.

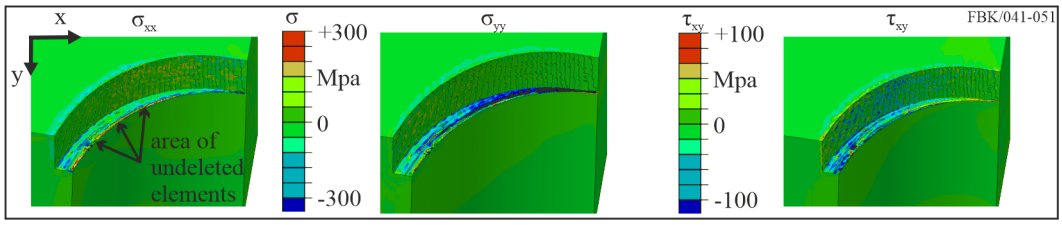

Figure 12 Deformed workpiece with residual stress distribution σ_{yy}.

3.4 Distortion analysis

The distortion analysis is divided into two sections. First the distortion of the simple wafer geometry is analyzed and discussed. After that, the distortion of the more complex feature geometry is investigated. For both geometries, the 3D linear elastic FEM model is first validated by using the measured residual stress data as an input and comparing the results to measured distortion. Next the MIRS from the cutting simulation are used as an input to analyze how the differences of MIRS from the cutting simulation compared to the measured MIRS effect the distortion prediction.

3.4.1 Wafer distortion analysis

Figure 13 shows the color maps of the measured wafer distortion at the bottom (extracted from sample ID 2) and the wafer distortion predicted by the linear elastic FEM model using the averaged MIRS from hole drilling measurements and the left over low IBRS as an input. The color maps mimic looking down at the top milled surface with positive distortion in the z-direction (into the surface). The machined surface becomes convex (∩-shaped) due to the compressive MIRS at the top milled surface. Its maximum distortion is found at the top left (0 mm, 0 mm) and bottom right corner (25 mm, 25 mm). This kind of twisted distortion is due to the shear RS, which cause a torsional moment in addition to the bending moment caused by the normal RS [2, 7]. Therefore, mainly the shear RS are responsible for the maximum distortion on this diagonal. The contour plots of the measured and simulated distortion match. Both show the previously described convex-shaped distortion on a similar level. The line plots in Fig. 13 represent the distortion on the two diagonals and highlight, that the maximum distortion of the experiment is not fully achieved by the simulation. 82 % of the maximum distortion found on the diagonal \ is reached by the simulation. The differences in distortion might be explained by the measurement inaccuracies of the HD technique and the RS induced by the EDM cutting, although the cutting parameters were chosen to minimize the stress induced during cutting.

In general, it can be concluded that this simulation type is able to predict the distortion of simple flat geometries due to MIRS from milling and left over IBRS with a good accuracy.

Figure 14 shows the measured distortion of the wafer compared to the predicted distortion when using the MIRS from the cutting simulation instead of the hole drilling data and the measured left over low IBRS. It can be seen that the simulated distortion shape is convex as well, but with lower magnitude and a rotated shape of the low distortion region at the center compared the to the measured distortion. The maximum distortion still is found on top left (0 mm, 0 mm) and bottom right corner (25 mm, 25 mm). But now only 33 % of the maximum measured distortion is reached by the simulation. The lower magnitude of distortion could be explained by the lower magnitude and penetration depth of simulated MIRS from the cutting simulation compared to experimental data (see Fig. 11). The reason for the rotated distortion behavior is the difference of the magnitude of simulated normal MIRS (MaxRS_{yy} = -180 MPa and MaxRS_{xx} = -50 MPa).

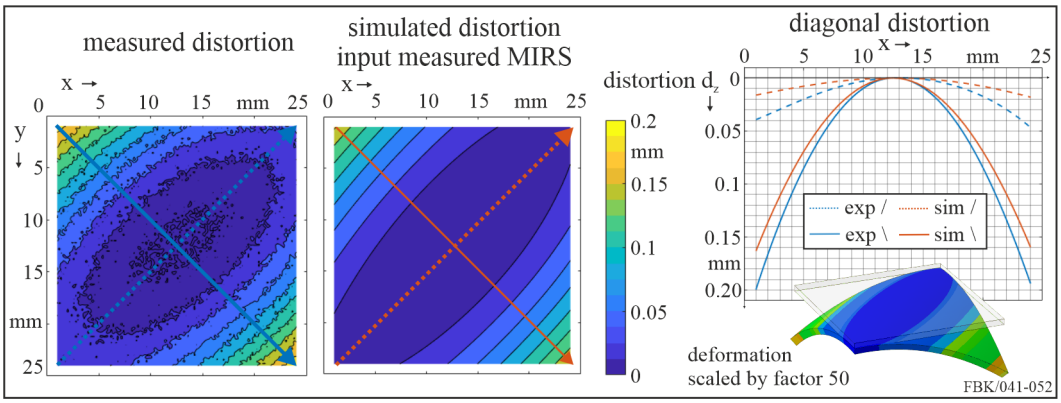

Figure 13 Measured and simulated wafer distortion with measured MIRS as input for simulation.

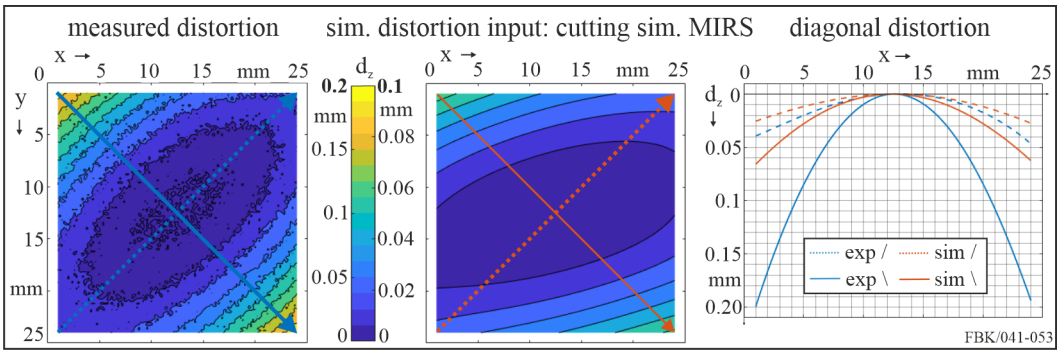

Figure 14 Measured and simulated wafer distortion with MIRS from cutting simulation as input.

3.4.2 Feature distortion analysis

Figure 15 shows the comparison of the measured distortion of the feature sample (at the backside) and the predicted distortion of the linear elastic FEM model due to the measured MIRS and low left over IBRS. The color maps mimic looking down at the milled surfaces of the pockets with positive distortion in the z-direction. Similar to the wafer distortion the maximum distortion can be found near the top left (0 mm, 0 mm) and bottom right corner (200 mm, 98 mm). In contrast to the wafer distortion the lowest level is not in the middle of the sample, which results in a X-shaped distortion. This is because of the more complex geometry of the feature sample with one rib and walls, which improve the stiffness of the geometry. Overall, the simulation is able to predict the shape of distortion, although it overestimates the maximum distortion in the corners by 132 % of the measured value (see Fig. 15). The differences in the measured and predicted distortion might be because only the MIRS at the bottom surface of the pockets and the left over IBRS are considered. Whereas in reality the machining of other surfaces such as the backside (step 2) or side walls (step 5) of the feature sample also induce low RS, which contribute to part distortion.

Figure 16 shows the measured distortion of the feature sample (at the backside) compared to the predicted distortion when using simulated MIRS and the measured left over low IBRS. Similar to the wafer distortion it can be stated that the MIRS from the cutting simulation as input lead to lower distortion than in reality (mind different scales in Fig. 16). Only 41 % of the maximum distortion found on the diagonal \ is reached by the simulation. But in general the simulated shape of distortion matches the experiments.

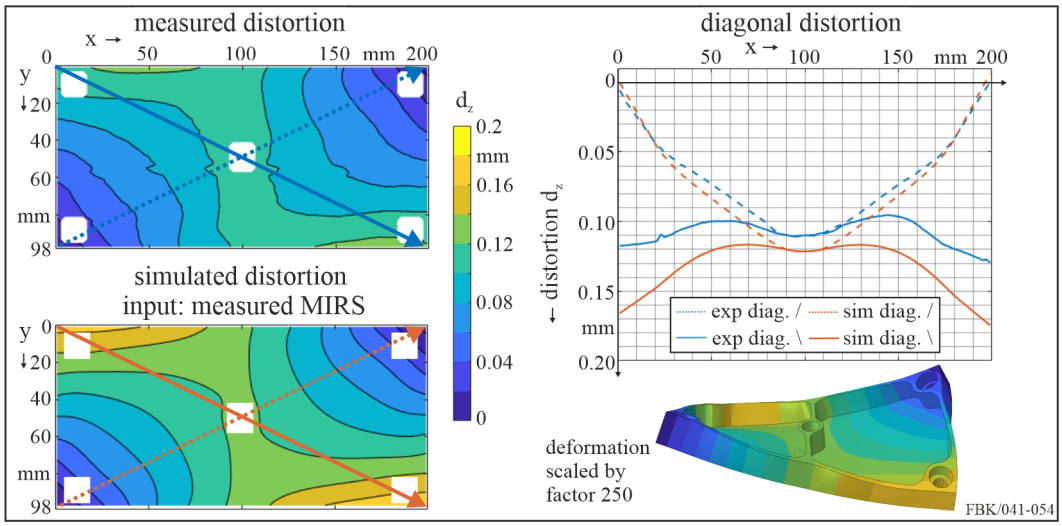

Figure 15 Measured and simulated feature distortion with measured MIRS as input.

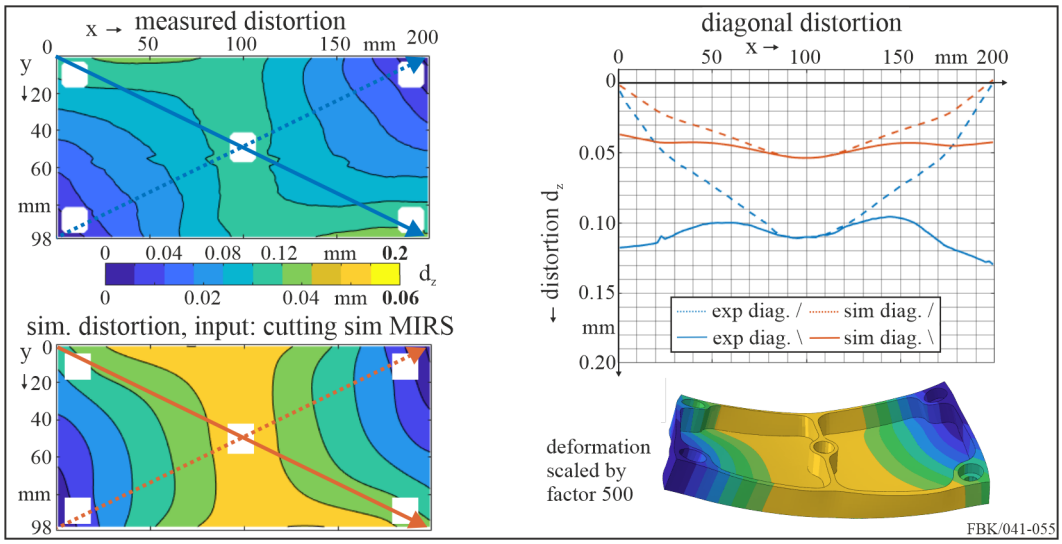

Figure 16 Measured and simulated feature distortion with MIRS from cutting sim. as input.

4 Conclusion and Outlook

The 3D, dynamic, elastic-plastic cutting FEM model was able to predict forces, temperatures and the MIRS profile with moderate accuracy. The depth profile of the MIRS with its typical square root-shape and the level of RS in general could be predicted qualitatively. But it also showed big deviations from reality in the form of lower penetration depth and lower values of the MaxRS (except in y-direction).

The linear elastic FEM model was able to predict the part distortion for simple (wafer) and more complex (feature) geometries qualitatively when using the measured MIRS and the left over low IBRS as input. In order to improve the simulation, MIRS at different surfaces need to be considered.

When combining both simulation models, the part distortion due to the simulated MIRS could not be predicted correctly, yet. Although the shape of distortion matches qualitatively, large deviations on the level of distortion are found, because of the deviations from the simulated MIRS from reality. This shows, that accurate MIRS are critical when used to predict distortion due to milling. Therefore, the cutting simulation needs some improvements. For example a finer resolution of the mesh, not only in the cutting zone, and the simulation of multiple tool rotations, to create a bigger MIRS analysis area and consider the run out of the tool, are necessary and will be investigated in future works. Furthermore, a deeper investigation on the used material models, e.g. a material flow stress curve optimization analysis similar to the approach presented by Eisseler et al. [4] could help to improve the results. Besides, the influence of the stable time increment, boundary conditions and friction model need to be investigated in detail. Moreover, the effect of different machining parameters used as an input for the cutting simulation on the MIRS and their distortion will be investigated.

References

1 Y. Bi, Q. Cheng, H. Dong, and Y. Ke. Machining distortion prediction of aerospace monolithic components. *Journal of Zhejiang University-SCIENCE A*, 10(5):667–668, 2009. doi:10.1631/jzus.A0820392.

2 C.R. Chighizola, C.R. D'Elia, D. Weber, B. Kirsch, J.C. Aurich, B.S. Linke, and M.R. Hill. Intermethod Comparison and Evaluation of Measured Near Surface Residual Stress in Milled Aluminum. *Currently under review in Expermintal Mechanics*, Submitted April 2020.

3 B. Denkena and S. Dreier. Simulation of residual stress related part distortion. In *New Production Technologies in Aerospace Industry - Proceedings of the 4th Machining Innovations Conference, Hannover, Germany*, pages 105–113, 2014. doi:10.1007/978-3-319-01964-2_15.

4 R. Eisseler, K. Drewle, K.C. Grötzinger, and H.C. Möhring. Using an inverse cutting simulation-based method to determine the johnson-cook material constants of heat-treated steel. In *Procedia CIRP 77 - Proceedings of the 8th CIRP Conference on High Performance Cutting*, pages 26–29, 2018. doi:10.1016/j.procir.2018.08.198.

5 K. Giasin, A. Hodzic, V. Phadnis, and S. Ayvar-Soberanis. Assessment of cutting forces and hole quality in drilling al2024 aluminium alloy: experimental and finite element study. *International Journal of Advanced Manufacturing Technolgy*, 87:2041–2061, 2016. doi:10.1007/s00170-016-8563-y.

6 P. Grant, J. Lord, P. Whitehead, and A.T. Fry. The Application of Fine Increment Hole Drilling for Measuring Machining-Induced Residual Stresses. *Applied Mechanics and Materials*, 3-4:105–110, 2005. doi:10.4028/www.scientific.net/AMM.3-4.105.

7 M. Gulpak, J. Sölter, and E. Brinksmeier. Prediction of shape deviations in face milling of steel. In *Procedia CIRP 8 - Proceedings of the 14th CIRP Conference on Modelling of Machining Operations*, pages 15–20, 2013. doi:10.1016/j.procir.2013.06.058.

8 M.R. Hill. The slitting method. In *Schajer GS (ed). Practical residual stress measurement methods. Wiley, West Sussex, UK*, 2013.

9 DMG Mori Homepage. https://de.dmgmori.com, last accessed 2020/08.

10 Mitsubishi Carbide Homepage. http://www.mitsubishicarbide.com, last accessed 2020/08.

11 X. Huang, X. Zhang, and H. Ding. An enhanced analytical modelof residual stress for peripheral milling. In *Procedia CIRP 58 - Proceedings of the 16th CIRP Conference on Modelling of Machining Operations*, pages 387–392, 2017. doi:10.1016/j.procir.2017.03.245.

12 X.M. Huang, J. Sun, and J.F. Li. Effect of initial residual stress and machining-induced residual stress on the deformation of aluminium alloy plate. *Journal of Mechanical Engineering*, 612:131–137, 2015. doi:10.5545/sv-jme.2014.1897.

13 X.M. Huang, J. Sun, and J.F. Li. Finite element simulation and experimental investigationon the residual stress-related monolithic component deformation. *International Journal of Advanced Manufacturing Technolgy*, 77:1035–1041, 2015. doi:10.1007/s00170-014-6533-9.

14 ASTM International. E837-13a Standard Test Method for Determining Residual Stresses by the Hole-Drilling Strain-Gage Method. West Conshohocken, PA:. *ASTM International*, 2013. doi:10.1520/E0837-13A.

15 S. Jayanti, D. Ren, E. Erickson, S. Usui, T. Marusich, K. Marusich, and H. Elanvogan. Predictive modeling for tool deflection andpart distortion of large machined components. In *Procedia CIRP 12 - Proceedings of the 8th CIRP Conference on Intelligent Computation in Manufacturing Engineering*, pages 37–42, 2013. doi:10.1016/j.procir.2013.09.008.

16 X. Jiang, Y. Zhu, Z. Zhang, M. Guo, and Z. Ding. Investigation of residual impact stress and its effects on the precision during milling of the thin-walled part. *International Journal of Advanced Manufacturing Technolgy*, 97:9–12, 2018. doi:10.1007/s00170-018-1941-x.

17 Z. Jiang, Y. Liu, L. Li, and W. Shao. A novel prediction model for thin plate deflections consideringmilling residual stresses. *International Journal of Advanced Manufacturing Technolgy*, 74:37–45, 2014. doi:10.1007/s00170-014-5952-y.

18 X. Jin. Mechanics and dynamics of micro-cutting process. In *Dissertation, The University of British Columbia-Vancouver*, 2012.

19 G.R. Johnson and W.H. Cook. Fracture characteristics of three metals subjected to various strains, strain rates, temperatures and pressures. *Engineering Fracture MEchanics*, 21(1):31–48, 1985.

20 D.R. Lesuer, G.J. Kay, and M.M. LeBlanc. Modeling large-strain, high-rate deformation in metals. In *Third Biennial Tri-Laboratory Engineering Conference Modeling and Simulation, Pleasanton, CA, November 3-5, 1999*, 2001.

21 B. Li, X. Jiang, J. Yang, and S. Liang. Effects of depth of cut on the redistribution of residual stress and distortion during the milling of thin-walled part. *Journal of Materials Processing Technology*, 216:223–233, 2015. doi:10.1016/j.jmatprotec.2014.09.016.

22 J.G. Li and S.Q. Wang. Distortion caused by residual stresses in machining aeronautical aluminum alloy parts: recent advances. *International Journal of Advanced Manufacturing Technolgy*, 89:997–1012, 2016. doi:10.1007/s00170-016-9066-6.

23 C.R. Liu and Y.B. Guo. Finite element analysis of the effect of sequential cuts and tool-chip friction on residual stresses in a machined layer. *International Journal of Mechanical Sciences*, 42:1069–1086, 2000. doi:10.1016/S0020-7403(99)00042-9.

24 Y. Ma, P.F. Feng, and D.W. Yu. Finite element analysis ofresidual stresses and thin plate distortion after face milling. In *Proceedings of 2015 12th International Bhurban Conference on Applied Sciences and Technology, Islamabad, Pakistan*, pages 67–71, 2015. doi:10.1109/IBCAST.2015.7058481.

25 A. Madariaga, I. Perez, P.J. Arrazola, R. Sanchez, J.J. Ruiz, and F.J. Rubio. Reduction of distortions in large aluminium parts by controlling machining-induced residual stresses. *International Journal of Advanced Manufacturing Technolgy*, 97:967–978, 2018. doi:10.1007/s00170-018-1965-2.

26 T.D. Marusich and M. Ortiz. Modelling and simulation of high-speed machining. *International Journal for Numerical Methods in Engineering*, 38:3675–3694, 1995. doi:10.1002/nme.1620382108.

27 J.K. Rai and P. Xirouchakis. Finite element method based machining simulation environment for analyzing part errors induced during milling of thin-walled components. *International Journal of Machine Tools and Manufacture*, 48:629–643, 2008. doi:10.1016/j.ijmachtools.2007.11.004.

28 V. Richter-Trummer, D. Koch, A. Witte, J.F. dos Sanos, and P.M.S.T. de Castro. Methodology for prediction of distortion of workpieces manufactured by high speed machining based on an accurate through-the-thickness residual stress determination. *International Journal of Advanced Manufacturing Technolgy*, 68:2271–2281, 2013. doi:10.1007/s00170-013-4828-x.

29 C. Shet and X. Deng. Residual stresses and strains in orthogonal metal cutting. *International Journal of Machine Tools and Manufacture*, 43:573–587, 2003. doi:10.1016/S0890-6955(03)00018-X.

30 W.M. Sim. Challenges of residual stress and part distortion in the civil airframe industry. *International Journal Microstructure and Material Properties*, 5:446–455, 2010. doi:10.1504/IJMMP.2010.037621.

31 Dassault Systems. Simulia ABAQUS 6.14 Abaqus/CAE User's Guide, 2014.

32 Dassault Systems. Simulia ABAQUS 6.14 Analysis User's Guide Volume III: Materials, 2014.

33 Z.T. Tang, T. Yu, L.Q. Xu, and Z.Q. Liu. Machining deformation prediction for frame componentsconsidering multifactor coupling effects. *International Journal of Advanced Manufacturing Technolgy*, 68:187–196, 2013. doi:10.1007/s00170-012-4718-7.

34 M. Wan, X. Ye Y. Yang, and W. Zhang. Theoretical prediction of machining-induced residual stresses in three-dimensional oblique milling processes. *International Journal of Mechanical Sciences*, 133:426–437, 2017. doi:10.1016/j.ijmecsci.2017.09.005.

35 F.Z. Wang, J. Sun, J. Zhou, and J.F. Li. Experiments and Finite Element Simulations on Micro-Milling of Aluminium Alloy 7050-T7451. *Advanced Material Research*, 500:556–562, 2012. doi:10.4028/www.scientific.net/AMR.500.556.

36 J. Wang, D. Zhang, B. Wu, and M. Luo. Numerical and empirical modelling of machining-induced residual stresses in ball end milling of Inconel 718. *Procedia CIRP 58 - Proceedings of the 16th CIRP Conference on Modelling of Machining Operations*, pages 7–12, 2017. doi:10.1016/j.procir.2017.03.177.

37 D. Weber, B. Kirsch, C.R. D'Elia, B.S. Linke, M.R. Hill, and J.C. Aurich. Concept to analyze residual stresses in milled thin walled monolithic aluminum components and their effect on part distortion. In *Production at the leading edge of technology - Proceedings of the 9th Congress of the German Academic Association for Production Technology*, pages 287–296, 2019. doi:10.1007/978-3-662-60417-5_29.

38 T. Özel and E. Zeren. Finite Element Method Simulation of Machining of AISI 1045 Steel With A Round Edge Cutting Tool . In *Proceedings of the 8th CIRP International Workshop on Modeling of Machining Operations, Chemnitz, Germany*, pages 533–542, 2005.